JOURNAL OF SPACECRAFT AND ROCKETS
Vol. 33, No. 6, November–December 1996

Computation of the Roll Characteristics of a Finned Projectile

Paul Weinacht* and Walter B. Sturek†
U.S. Army Research Laboratory, Aberdeen Proving Ground, Maryland 21005-5066

A computational technique has been developed and applied to predict the aerodynamic roll characteristics of a finned projectile. These aerodynamic parameters include the roll-producing moment, the roll-damping moment, and the equilibrium spin rate, defined as the spin rate for which the net roll moment is zero. The roll characteristics have been determined by computing the flowfield about the projectile using a parabolized Navier–Stokes computational approach. Because the body is not axisymmetric, a body-fixed rotating coordinate frame is employed to remove the time-dependency from the computation. The governing equations are appropriately modified to include the Coriolis and centrifugal accelerations resulting from the rotating coordinate frame. Comparison is made with results obtained experimentally from range firings and from engineering estimation approaches. The computed equilibrium spin rate and the spin histories agree well with the data obtained from range firings. The results likely represent the first known application of Navier–Stokes techniques for predicting the roll characteristic of nonaxisymmetric bodies.

Nomenclature

a_∞ = freestream speed of sound
C_D = drag coefficient
C_l = roll moment coefficient
C_{l_o} = roll-producing moment coefficient
C_{l_p} = roll-damping moment coefficient
$c(r)$ = local chord length of fin
D = projectile diameter
$\hat{E}, \hat{F}, \hat{G}$ = flux vectors in transformed coordinates
e = total energy per unit volume, nondimensionalized by $\rho_\infty a_\infty^2$
$\hat{H}$ = source term resulting from rotating coordinate frame
$\hat{H}_c$ = inviscid source term resulting from the cylindrical coordinate formulation
I = moment of inertia
J = Jacobian
M_∞ = freestream Mach number
m = projectile mass
N_{fins} = number of fins
p = pressure, as used in thin-layer Navier–Stokes equations, nondimensionalized by $\rho_\infty a_\infty^2$
p = spin rate, as used roll equations and aerodynamic coefficients
p_∞ = freestream static pressure
pD/V = nondimensional spin rate
$(pD/V)_0$ = initial nondimensional spin rate
$(pD/V)_{ss}$ = nondimensional steady-state spin rate
Re = Reynolds number
r = radial coordinate
$\hat{S}$ = viscous flux vector in transformed coordinates
$\hat{S}_c$ = viscous source term resulting from cylindrical coordinate formulation
S_{ref} = reference cross-sectional area of projectile, $\pi D^2/4$
s = distance downrange
t = time
U, V, W = contravariant velocities of the transformed Navier–Stokes equations
u, v, w = axial, tangential, and normal velocity components of the Navier–Stokes equations, nondimensionalized by a_∞
V = freestream velocity used to nondimensionalize the spin rate and the aerodynamic coefficients
γ = ratio of specific heats
$\delta(r)$ = local cant angle of fin
μ = laminar viscosity
μ_t = turbulent viscosity
ξ, η, ζ = transformed coordinates
ρ = density, nondimensionalized by ρ_∞
ρ_∞ = freestream density
Ω = angular velocity of the rotating frame nondimensionalized by a_∞/D

Received Feb. 7, 1996; revision received June 20, 1996; accepted for publication June 26, 1996.

*Aerospace Engineer, Aerodynamics Branch, Propulsion and Flight Division, Weapons Technology Directorate. Senior Member AIAA.

†Senior Scientist, High Performance Computing Division, Advanced Simulation and High Performance Computing Directorate. Associate Fellow AIAA.

Introduction

THE ability to accurately predict the roll characteristics of projectiles is important to the projectile designer. Although spin is not required to maintain stability for a statically stable projectile, rolling the projectile at a low spin rate can minimize the effect of aerodynamic and inertial asymmetries on the free-flight trajectory. A good design will have an equilibrium spin rate that avoids both the yawing frequency and the projectile's first natural frequency of vibration. The yawing frequency is avoided to preclude the possibility of spin/yaw lock in, which may lead to increases in yaw during flight. If the flight body experiences spin rates near the first natural frequency of vibration, bending of the body may occur. Typically, the natural frequency and the yawing frequency represent an upper and lower bound for the design equilibrium spin rate.

The roll behavior of a flight vehicle can be characterized by the roll-producing moment coefficient, the roll-damping moment coefficient, and the equilibrium spin rate, defined as the spin rate for which the net roll moment is zero. Although the prediction of the roll-producing moment is conceptually straightforward because the moment is produced in the absence of spin, the roll-damping moment requires predictions of the roll moment in the presence of spin. Spin, when combined with angle of attack, produces a time-dependent but periodic flowfield for nonaxisymmetric bodies. However, at zero degrees angle of attack, a steady flowfield on a spinning nonaxisymmetric body can be observed from a body-fixed coordinate frame. The body-fixed frame can be utilized to predict the flowfield provided the governing equations are modified to incorporate the centrifugal and Coriolis body forces resulting from the noninertial coordinate frame. The use of a body-fixed rotating coordinate frame is the basis of the current computational approach for predicting the roll characteristics for nonaxisymmetric bodies at zero degrees angle of attack. This allows a steady flow approach

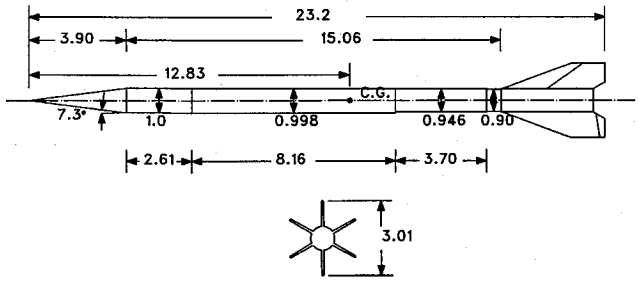

Fig. 1 Schematic of the finned projectile. All dimensions are in calibers (one caliber = 27.05 mm).

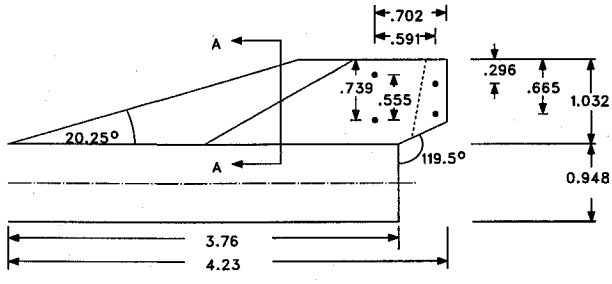

Fig. 2 Schematic of fin planform. All dimensions are in calibers (one caliber = 27.05 mm).

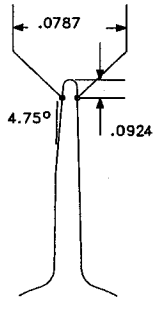

Fig. 3 Detail of fin leading edge.

Section A-A

based on the parabolized Navier–Stokes equations to be applied to determine the aerodynamic parameters of interest in a cost-effective manner.

Prior to the development of the current approach, only the roll-producing moment had been determined for nonaxisymmetric bodies using Euler or Navier–Stokes computational methods.[1] To determine the roll-damping moment coefficient or the steady-state spin rate, projectile designers relied on approximate methods for predictions. These methods included analytical[2,3] or empirical[4,5] approaches or computational methods based on approximate solutions of the Euler equations.[6] The current method provides a method of predicting both the roll-producing and the roll-damping moment coefficients and steady-state spin rate using a method that is readily adapted to existing computational fluid dynamics codes.

The current approach is applied to predict the roll characteristics of a finned projectile. A schematic of the projectile is shown in Figs. 1–4. The particular fin design shown here has roll-producing beveled surfaces at the leading and trailing edge of the fins. The computational approach is applied to predict the roll-producing and roll-damping moment coefficients and the steady-state spin rate over a range of supersonic Mach numbers. Comparison is made with results obtained experimentally from range firings and from engineering estimation approaches.

The equation of motion for a projectile undergoing pure rolling motion is briefly discussed in the next section. The computational techniques used to predict the roll characteristics are then presented, followed by a brief discussion of the range data and engineering estimation approach. Presentation and discussion of the results obtained by applying these techniques is then made and, finally, the conclusions of this study are presented.

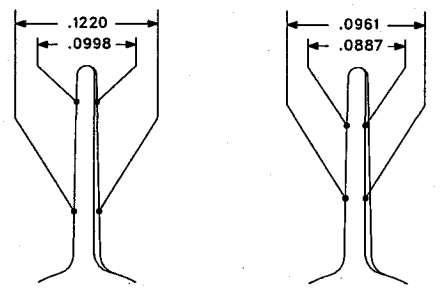

Fig. 4 Detail of fin trailing edge.

Roll Equation

Aeroballisticians describe the spin history of the projectile in terms of the following ordinary differential equation[7]:

$$I\frac{dp}{dt} = \frac{1}{2}\rho_\infty a_\infty^2 M_\infty^2 D S_{\text{ref}} C_l \tag{1}$$

The net aerodynamic roll moment is composed of two components, the roll-producing moment and the roll-damping moment. The roll-producing moment, which induces spin on the projectile, results from the aerodynamic loads produced by either the machined asymmetries in the fin geometry or by the fin cant, whereas the roll-damping contribution consists of pressure and viscous forces that oppose the spin. The relationship of these contributions to the net aerodynamic roll moment is expressed in nondimensional form:

$$C_l = C_{l_o} + C_{l_p}(pD/V) \tag{2}$$

The roll-damping coefficient will differ in sign with the roll-producing moment coefficient and will be negative if the direction of positive roll moment is in the direction of positive spin.

In the computational frame work, where the projectile is flying at constant velocity, Eq. (2) shows that the roll-producing moment can be obtained by computing the net aerodynamic roll moment at zero spin rate. Likewise, the roll-damping moment is obtained by computing the net aerodynamic roll moment on the projectile at a fixed spin rate, subtracting the roll-producing moment from it and dividing by the spin rate. The equilibrium spin rate, which occurs when the net aerodynamic roll moment is zero, is obtained by dividing the roll-producing moment coefficient by the roll-damping moment coefficient and changing the sign.

A closed-form solution[7] of Eq. (1) can be obtained by transforming the independent variable from time to distance and by assuming that the aerodynamic coefficients do not vary across the Mach number range of interest. In transforming the independent variable from time to distance, solution of the drag equation is implicitly included. The solution of this equation is

$$pD/V = (pD/V)_0 + [(pD/V)_{\text{ss}} - (pD/V)_0][1 - e^{-K_p s/D}] \tag{3}$$

where

$$K_p = -\frac{\rho_\infty S_{\text{ref}} D}{2m}\left[C_D + k_a^{-2} C_{l_p}\right] \qquad K_\delta = \frac{\rho_\infty S_{\text{ref}} D^3}{2I} C_{l_o}$$
$$k_a = \sqrt{I/mD^2} \qquad (pD/V)_{\text{ss}} = K_\delta / K_p \tag{4}$$

The spin rate at launch $(pD/V)_0$ represents an initial condition, which must be specified. In the analysis presented here, the spin rate at launch is presumed to be zero. Note that the steady-state spin rate $(pD/V)_{\text{ss}}$, differs slightly from the equilibrium spin rate already defined in that the drag term appears in the definition of the steady-state spin rate. For the case of zero drag (projectile is flying at constant velocity), the steady-state spin rate becomes identical to the equilibrium spin rate. The difference between the equilibrium spin rate and the steady-state spin rate is about one-half of 1% for the projectile examined here.

Computational Approach

Computation of the viscous flowfield about the finned projectile configurations was accomplished by solving the thin-layer Navier–Stokes equations using a parabolized Navier–Stokes technique. The computations have been performed in a novel rotating coordinate frame that rotates at the spin rate of the projectile. The fluid flow relative to the rotating coordinate frame does not vary with time, allowing the steady (nontime varying) Navier–Stokes equations to be applied. The solution of the steady Navier–Stokes equations can be performed at a reasonable computational cost. To implement the rolling coordinate frame, the governing equations have been modified to include the effect of centrifugal and Coriolis forces. The steady thin-layer Navier–Stokes equations written in generalized coordinates are[8]

$$\frac{\partial \hat{E}}{\partial \xi}+\frac{\partial \hat{F}}{\partial \eta}+\frac{\partial \hat{G}}{\partial \zeta}+\hat{H}_c+\hat{H}=\frac{1}{Re}\left(\frac{\partial \hat{S}}{\partial \zeta}+\hat{S}_c\right) \tag{5}$$

Here, $\hat{E}$, $\hat{F}$, and $\hat{G}$ are the inviscid flux vectors, $\hat{S}$ is the viscous flux vector, $\hat{H}_c$ and $\hat{S}_c$ are inviscid and viscous source terms resulting from the cylindrical coordinate formulation, and $\hat{H}$ is the source term containing the Coriolis and centrifugal force terms, which result from the rotating coordinate frame. Each of these matrices are functions of the dependent variables represented by the vector $q(\rho, \rho u, \rho v, \rho w, e)$. The flux terms are

$$\hat{E}=\frac{1}{J}\begin{bmatrix}\rho U\\ \rho uU+\xi_x p\\ \rho vU\\ \rho wU\\ (e+p)U\end{bmatrix}\qquad \hat{F}=\frac{1}{J}\begin{bmatrix}\rho V\\ \rho uV+\eta_x p\\ \rho vV+\eta_\theta p/r\\ \rho wV+\eta_r p\\ (e+p)V\end{bmatrix}$$

$$\hat{G}=\frac{1}{J}\begin{bmatrix}\rho W\\ \rho uW+\zeta_x p\\ \rho vW+\zeta_\theta p/r\\ \rho wW+\zeta_r p\\ (e+p)W\end{bmatrix}\qquad \hat{H}_c=\frac{1}{Jr}\begin{bmatrix}\rho w\\ \rho uw\\ 2\rho vw\\ \rho(w^2-v^2)\\ (e+p)w\end{bmatrix} \tag{6}$$

$$\hat{S}=\frac{1}{J}\begin{bmatrix}0\\ m_1\dfrac{\partial u}{\partial \zeta}+m_2\zeta_x\\ m_1\dfrac{\partial v}{\partial \zeta}+\dfrac{m_2\zeta_\theta}{r}\\ m_1\dfrac{\partial w}{\partial \zeta}+m_2\zeta_r\\ m_3\end{bmatrix}\qquad \hat{H}=\frac{1}{J}\begin{bmatrix}0\\ 0\\ 2\Omega\rho w\\ -2\Omega\rho v-\Omega^2 r\rho\\ -\Omega^2 r\rho w\end{bmatrix}$$

where

$$U=u\xi_x \qquad V=u\eta_x+v\eta_\theta/r+w\eta_r$$
$$W=u\zeta_x+v\zeta_\theta/r+w\zeta_r \tag{8}$$
$$m_1=(\mu+\mu_t)\left[\zeta_x^2+(\zeta_\theta/r)^2+\zeta_r^2\right]$$
$$m_2=\frac{1}{3}(\mu+\mu_t)\left(\zeta_x\frac{\partial u}{\partial \zeta}+\frac{1}{r}\zeta_\theta\frac{\partial v}{\partial \zeta}+\zeta_r\frac{\partial w}{\partial \zeta}\right) \tag{9}$$
$$m_3=\frac{1}{\gamma-1}\left(\frac{\mu}{Pr}+\frac{\mu_t}{Pr_t}\right)\left[\zeta_x^2+\left(\frac{\zeta_\theta}{r}\right)^2+\zeta_r^2\right]\frac{\partial a^2}{\partial \zeta}$$
$$+\frac{1}{2}m_1\frac{\partial q^2}{\partial \zeta}+m_2\left(u\zeta_x+\frac{v}{r}\zeta_\theta+w\zeta_r\right)$$
$$a^2=\gamma p/\rho \tag{10}$$
$$q^2=u^2+v^2+w^2 \tag{11}$$
$$\xi_x=1/x_\xi \qquad \eta_x=J(r_\xi\theta_\zeta-\theta_\xi r_\zeta) \qquad \eta_\theta=J(x_\xi r_\zeta)$$
$$\eta_r=J(-x_\xi\theta_\zeta) \qquad \zeta_x=J(\theta_\xi r_\eta-r_\xi\theta_\eta) \tag{12}$$
$$\zeta_\theta=J(-x_\xi r_\eta) \qquad \zeta_r=J(x_\zeta\theta_\eta) \qquad J=\frac{1}{x_\xi(\theta_\eta r_\zeta-\theta_\zeta r_\eta)}$$

The pressure p can be related to the dependent variables by applying the ideal gas law,

$$p=(\gamma-1)[e-(\rho/2)q^2] \tag{13}$$

The turbulent viscosity μ_t, which appears in the viscous matrices, was computed using the Baldwin–Lomax turbulence model.[9]

The thin-layer equations are solved using the parabolized Navier–Stokes technique of Schiff and Steger.[8] Following the approach of Schiff and Steger, the governing equations, which have been modified here to include the Coriolis and centrifugal force terms, are solved using a conservative, approximately factored, implicit finite difference numerical algorithm as formulated by Beam and Warming.[10]

The equations are first linearized and placed in delta form, where the equations are solved for the difference in the dependent variables rather than the variable itself. This set of equations is then factorized

$$\hat{S}_c=\frac{1}{J}\begin{bmatrix}0\\ -\zeta_x\dfrac{\partial}{\partial \zeta}\left[(\mu+\mu_t)\dfrac{2w}{3r}\right]+\dfrac{\mu+\mu_t}{r}\left(\zeta_r\dfrac{\partial u}{\partial \zeta}+\zeta_x\dfrac{\partial w}{\partial \zeta}\right)\\ -\zeta_r\dfrac{\partial}{\partial \zeta}\left[(\mu+\mu_t)\dfrac{v}{r}\right]+\dfrac{\zeta_\theta}{r}\dfrac{\partial}{\partial \zeta}\left[(\mu+\mu_t)\dfrac{4w}{3r}\right]+\dfrac{2(\mu+\mu_t)}{r}\left(\dfrac{\zeta_\theta}{r}\dfrac{\partial w}{\partial \zeta}+\zeta_r\dfrac{\partial v}{\partial \zeta}-\dfrac{v}{r}\right)\\ -\dfrac{\zeta_\theta}{r}\dfrac{\partial}{\partial \zeta}\left[(\mu+\mu_t)\dfrac{v}{r}\right]-\zeta_r\dfrac{\partial}{\partial \zeta}\left[(\mu+\mu_t)\dfrac{2w}{3r}\right]+\dfrac{2(\mu+\mu_t)}{r}\left(\dfrac{-\zeta_\theta}{r}\dfrac{\partial v}{\partial \zeta}+\zeta_r\dfrac{\partial w}{\partial \zeta}-\dfrac{w}{r}\right)\\ -\zeta_x\dfrac{\partial}{\partial \zeta}\left[(\mu+\mu_t)\dfrac{2uw}{3r}\right]+\dfrac{\zeta_\theta}{r}\dfrac{\partial}{\partial \zeta}\left[(\mu+\mu_t)\dfrac{vw}{3r}\right]-\dfrac{\zeta_r}{r}\dfrac{\partial}{\partial \zeta}\left[(\mu+\mu_t)\left(v^2+\dfrac{2}{3}w^2\right)\right]+\dfrac{(\mu+\mu_t)\zeta_r}{2r}\dfrac{\partial}{\partial \zeta}(q^2)\\ -\dfrac{2w(\mu+\mu_t)}{3r}\left(\zeta_x\dfrac{\partial u}{\partial \zeta}+\dfrac{\zeta_\theta}{r}\dfrac{\partial v}{\partial \zeta}+\zeta_r\dfrac{\partial w}{\partial \zeta}\right)+\dfrac{(\mu+\mu_t)}{r}\left(u\zeta_x\dfrac{\partial w}{\partial \zeta}+\dfrac{v\zeta_\theta}{r}\dfrac{\partial w}{\partial \zeta}+w\zeta_r\dfrac{\partial w}{\partial \zeta}\right)+\dfrac{1}{\gamma-1}\left(\dfrac{\mu}{Pr}+\dfrac{\mu_t}{Pr_t}\right)\zeta_r\dfrac{\partial}{\partial \zeta}(a^2)\end{bmatrix} \tag{7}$$

using the approach of Beam and Warming.[10] The following set of equations, where RHS is the right-hand side, is obtained:

$$\left[\tilde{A}_s^j + (1-\alpha)\Delta\xi\left(\delta_\eta \tilde{B}^j + \tilde{D}^j + \tilde{D}_c^j\right)\right]\Delta\hat{q}^* = \text{RHS} \tag{14}$$

$$\left\{\tilde{A}^j + (1-\alpha)\Delta\xi\left[\delta_\zeta \tilde{C}^j - (1/Re)\left(\delta_\zeta \tilde{M}^j + \tilde{M}_c^j\right)\right]\right\}\Delta\hat{q}^j = \tilde{A}_s^j \Delta\hat{q}^* \tag{15}$$

$$\begin{aligned}\text{RHS} = &-\left(\tilde{A}_s^j - \tilde{A}_s^{j-1}\right)\hat{q}^j + \alpha\left(\hat{E}_s^j - \hat{E}_s^{j-1}\right) \\ &- \left[(\xi_x/J)^{j+1}E_p^j - (\xi_x/J)^j E_p^{j-1}\right] \\ &- (1-\alpha)\Delta\xi\left\{\delta_\eta\left[\eta_x^{j+1}(E/J)^j + (\eta_\theta/r)^{j+1}(F/J)^j\right.\right. \\ &\left.\left. + \eta_r^{j+1}(G/J)^j\right] + \delta_\zeta\left[\zeta_x^{j+1}(E/J)^j + (\zeta_\theta/r)^{j+1}(F/J)^j\right.\right. \\ &\left.\left. + \zeta_r^{j+1}(G/J)^j\right] + \hat{H}^j + \hat{H}_c^j - (1/Re)\left(\delta_\zeta \tilde{S}^j + \tilde{S}_c^j\right)\right\}\end{aligned} \tag{16}$$

The form of the equations, as well as the notation, is similar to that used by Schiff and Steger.[8] Here, $\tilde{A}$, $\tilde{B}$, $\tilde{C}$, and $\tilde{M}$ are the Jacobian matrices of the flux vectors $\hat{E}$, $\hat{F}$, $\hat{G}$, and $\hat{S}$. Further details on the definitions of these matrices can be found in Ref. 8. The important difference here is the addition of the matrices $\tilde{D}$ and $\hat{H}$ resulting from the rotating coordinate system. Although the Jacobian matrix $\tilde{D}$ can be included in either the circumferential inversion or in the normal inversion, including this term in the circumferential inversion simplifies slightly the implementation of the shock fitting boundary conditions.

The computations presented here were performed using a shock fitting procedure.[11] This procedure solves the five Rankine–Hugoniot jump conditions, two geometric shock-propagation conditions, and one compatibility equation to determine the values of the five dependent variables immediately behind the shock, as well as the position of the shock. By including the implicit part of the source term resulting from the rotating coordinate frame in the circumferential inversion, the shock fitting procedure of Rai and Chaussee[11] can be used without modification, as long as the correct freestream conditions are specified as shown in nondimensional form:

$$\rho = 1 \qquad \rho u = M_\infty \qquad \rho v = r\Omega \qquad \rho w = 0$$
$$e = 1/[\gamma(\gamma-1)] + \tfrac{1}{2}\left\{M_\infty^2 + r^2\Omega^2\right\} \tag{17}$$

The computational results presented here were obtained using a grid that consisted of 60 points between the body and the shock. In the circumferential direction, gridding was performed over a 60-deg sector because of the periodic symmetry present in the configuration examined here. Over the forebody, six circumferential points were used, though the flow here is axisymmetric. On the finned portion of the body, 50 points were used in the circumferential direction. The grid over this part of the body was generated using an elliptic grid generation scheme.[12] Marching step sizes of 0.0188 and 0.0094 body diameters were utilized over the axisymmetric and finned portions of the body, respectively. Solutions over the axisymmetric and finned portion of the body were obtained in 250 and 1100 s, respectively, on a Cray 2 supercomputer.

To ensure grid independent solutions were obtained using the baseline grid, fine grid computations were performed by doubling the number of grid points in the circumferential, normal, and longitudinal directions. The differences between the baseline and fine grid predictions of the computed roll-producing moment coefficient, roll-damping moment coefficient, and steady-state spin rates were less than 1.5%.

The surface grid was obtained using an analytical description of the projectile geometry. Particular care was taken to accurately model the roll producing surfaces on the fin geometry. It should be noted that the fins on this projectile overhang the base. This aspect of the projectile was modeled by extending the base so that it was aligned with the trailing edge of the fins. This allowed the flowfield to be computed up to the trailing edge of the fins. However, when the pressure and viscous stresses were integrated to compute the forces acting on the body, the contribution from this part of the body was not considered. Because the flow is supersonic and the fins are not immersed in the recirculating flow in the base, the flowfield adjacent to this region can be considered to be reasonably well modeled. Though not shown in Fig. 1, the cylindrical portion of the body has a number of circumferential grooves that cover nearly two-thirds of the body. The effect of these grooves is not modeled in the current computations, though it is a subject of current research.

Fig. 5 Cross-sectional view of fin showing cant angle.

Engineering Estimation Approach

Two simple approaches have been formulated to estimate the roll-producing and roll-damping moments, and subsequently, the equilibrium spin rate. These approaches are typical of the approaches currently adopted by some projectile designers.

Estimation of the Roll Damping of Finned Projectile

One approach for estimating the roll damping of a finned projectile is to use a strip-theory approach, breaking the fin planform into many small chordwise strips.[13] Each strip is assumed to be a two-dimensional flat plate at angle of attack, where the local angle of attack is a function of the local circumferential velocity resulting from the spin and the axial component of the velocity. The lift on each strip can be determined using supersonic thin airfoil theory.[14] The roll moment is then determined by integrating the lift on each strip multiplied by the local moment arm. Note that the sign of the roll moment will be negative since the roll moment opposes the spin. The roll-damping moment, which is the variation in the roll moment with spin, can be determined by dividing the roll moment by the nondimensional spin rate, since roll moment on the flat-plate fin will be zero at zero spin rate. The resulting equation for the roll-damping moment coefficient is

$$C_{l_p} = \frac{-16N_{\text{fins}}}{\pi\sqrt{M_\infty^2 - 1}} \int_{r_{\text{root}}/D}^{r_{\text{tip}}/D} \frac{c(r/D)}{D}\left(\frac{r}{D}\right)^2 \text{d}\left(\frac{r}{D}\right) \tag{18}$$

Estimation of the Roll-Producing Moment on a Beveled Fin

The roll-producing moment caused by the machined asymmetries on the leading and trailing edges of the fin can be estimated using an approach similar to that applied to estimate the roll-damping moment. Strip theory is again applied, and the fin is treated as a two-dimensional flat plate at angle of attack, where the local angle of attack is equal to the local cant angle, $\delta(r/D)$. The cant angle of the fin results because of the deflection of the leading and trailing edges of the fins resulting from the beveling. The cant angle is shown schematically in Fig. 5. The roll-producing moment is determined by integrating the lift on each strip multiplied by the local moment arm. As before, the lift on each strip is determined from thin airfoil theory. The resulting integral expression for the roll-producing moment coefficient is

$$C_{l_o} = \frac{16N_{\text{fins}}}{\pi\sqrt{M_\infty^2 - 1}} \int_{r_{\text{root}}/D}^{r_{\text{tip}}/D} \frac{c(r/D)\delta(r/D)}{D}\left(\frac{r}{D}\right)\text{d}\left(\frac{r}{D}\right) \tag{19}$$

Range Results

During 1983, 11 surrogate projectiles were fired through the Ballistic Research Laboratory Transonic Range.[15] The launch Mach number of the rounds varied between 3.5 and 5.25. The in-flight motion of the rounds was measured, including the spin rates at two stations along the trajectory. Spin card arrays were used to measure the projectile spin rate.

Using the closed-form solution of the roll equation [Eq. (3)], a fit of the projectile's rolling motion was obtained for each of the rounds. Since rounds fired from a smooth-bore gun typically have nearly zero initial spin rate, the initial spin rate was assumed to be zero. With the initial spin rate specified, the roll equation

contains two additional parameters, K_p and $(pD/V)_{ss}$, which were fit uniquely using the spin data obtained at the two measurement stations. The roll-producing and roll-damping moment coefficients were then extracted from these parameters using Eq. (4). The drag coefficient used in extracting the roll-damping moment coefficient was obtained from the range reduction.[15]

Results

Computations have been performed to predict the following aerodynamic parameters that determine the roll characteristics of the finned projectile: the roll-producing moment, the roll-damping moment, and the equilibrium spin rate. The computations were performed over a range of Mach numbers ($M = 3.0-5.5$) and nondimensional spin rates ($pD/V = 0-0.015$) for free-flight (sea-level) atmospheric conditions. The computed roll characteristics were compared with values determined from engineering estimation approaches and with results obtained from range firings. Roll histories were obtained by solving the roll equation using the computed aerodynamic roll moment coefficients and were compared with the range measurements. In this section, the computational and engineering approach results are first presented, followed by the comparisons of the computational results with the range results.

Computational and Engineering Approach Results

The roll-producing moment is obtained by computing the net roll moment at zero spin rate. Figure 6 shows the development of the roll-producing moment coefficient as it is integrated down the body at Mach 4. The roll-producing moment initially shows a rapid increase over the front of the fin because of the leading edge bevel. At axial locations near the aft end of the leading-edge bevel (and upstream of the trailing-edge bevel) the roll moment decreases somewhat because of a pressure differential across the fin that opposes the roll moment component from the leading-edge bevel. The roll moment begins to increase again at axial locations where the trailing-edge bevel exists.

Figure 7 shows the pressure distribution on both sides of the fin at a spanwise location which is halfway between the root and tip chords.

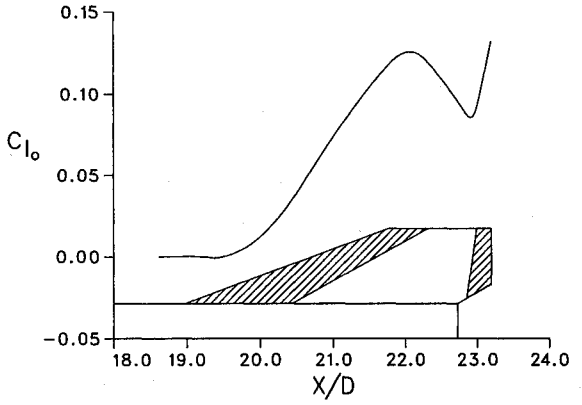

Fig. 6 Development of roll-producing moment coefficient over fins, Mach = 4.

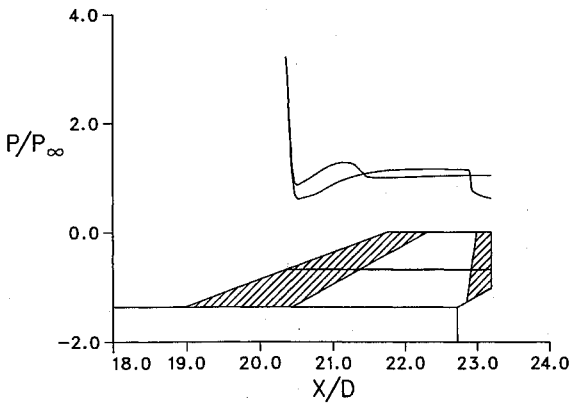

Fig. 7 Pressure distribution on fin at midspan, Mach 4.

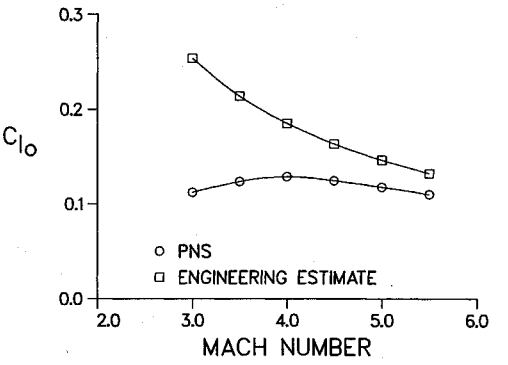

Fig. 8 Variation of engineering and computed predictions of roll-producing moment coefficient with Mach number.

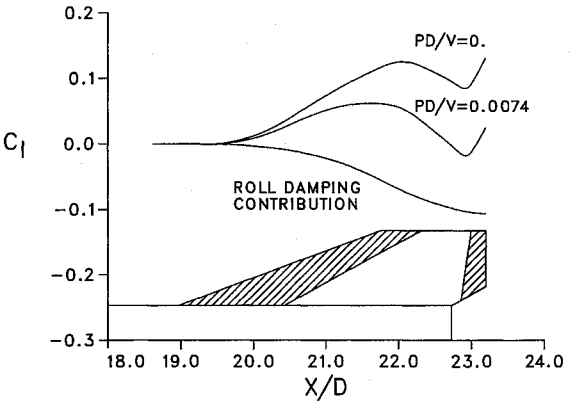

Fig. 9 Development of net roll moment coefficient over fins, Mach 4.

This pressure profile is typical of other spanwise locations. The roll-producing pressure differentials from the leading- and trailing-edge bevels are evident, as well as the opposing pressure differential between the two bevels.

The computed roll-producing moment coefficient as a function of Mach number is shown in Fig. 8. Also shown are the results from the engineering approach. The computed results show that the roll-producing moment has a maximum value at Mach 4. The decrease in the roll-producing moment below Mach 4 is because of the increasing role of the pressure differential downstream of the leading-edge bevel that opposes the roll-producing contributions from the leading- and trailing-edge bevels. This behavior is not predicted by the engineering approach, which shows an asymptotic behavior with Mach number. Above Mach 4, both approaches show a similar variation with Mach number because of the decreasing effectiveness of the roll producing surfaces. The engineering approach consistently overpredicts the roll-producing moment by 25–100%.

The development of the net roll moment acting on the body at nondimensional spin rates of 0 and 0.0074 is shown in Fig. 9. The difference between these two curves is the roll-damping contribution to the net roll moment. This difference is also shown. The magnitude of the roll-damping contribution shows a rapid increase over the swept portion of the fin. On the aft portion of the fin, where the fin has reached its maximum span, the roll-damping contribution does not increase as rapidly. This is in part because of tip effects, which become more pronounced at the lower Mach numbers considered here.

The variation of the net roll moment with spin rate at Mach 4 is shown in Fig. 10. For the range of spin rates of interest in the current study, the net roll moment exhibits a linear variation with spin rate. The slope of this curve represents the roll-damping moment coefficient, since the roll-damping moment is, by definition, the variation of net roll moment with spin rate.

The variation of the computed roll-damping moment coefficient with Mach number is seen in Fig. 11 along with results from the engineering approach. The computed roll-damping moment coefficient has a maximum at about Mach 4 and decreases slightly below Mach 4, because of tip effects. The engineering approach shows an asymptotic decrease in the roll-damping moment with increasing

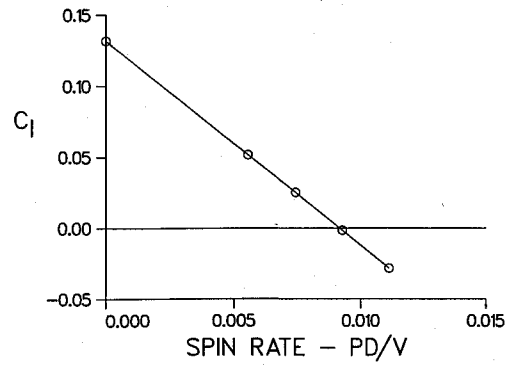

Fig. 10 Variation of net roll moment coefficient with spin rate, Mach 4.

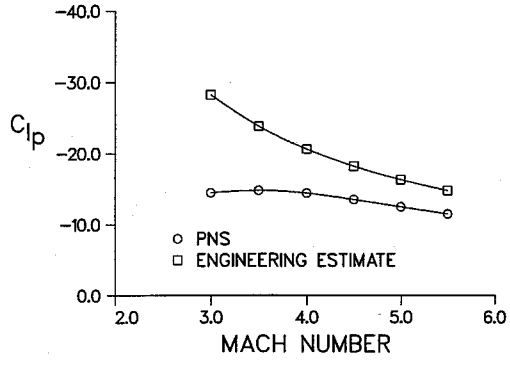

Fig. 11 Variation of engineering and computed predictions of roll-damping moment coefficient with Mach number.

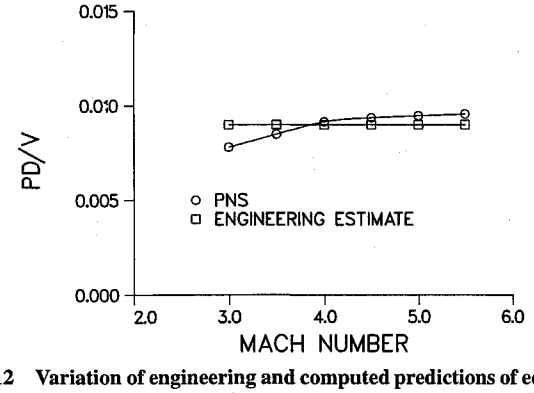

Fig. 12 Variation of engineering and computed predictions of equilibrium spin rate with Mach number.

Mach number because of the decreasing effectiveness of the fin. This behavior is also seen in the computed results above Mach 4. As with the roll-producing moment results, the engineering approach consistently overpredicts the roll-damping moment by 25–100%.

Figure 10 also shows that at Mach 4, the net roll moment is zero at a nondimensional spin rate 0.0091. This spin rate is the equilibrium spin rate because the roll-producing moment is balanced by the roll-damping moment. The variation of the equilibrium spin rate with Mach number is shown in Fig. 12. The computed equilibrium spin rate shows little variation with Mach number at the higher Mach numbers. Below Mach 4, the equilibrium spin rate shows a slight decrease with decreasing Mach number, because the roll-producing moment coefficient is decreasing faster than the roll-damping moment coefficient. The engineering estimate of the equilibrium spin rate is independent of the Mach number because the roll-producing and roll-damping moment coefficients exhibit the same variation with Mach number. The engineering results are within 15% of the computed results.

Comparison with Range Results

Using the computed roll-producing and roll-damping moment coefficients, spin histories of the projectile were determined by solving the roll equation [Eq. (3)]. Spin trajectories were obtained for four launch Mach numbers, 3.5, 4.0, 4.65, and 5.25, corresponding closely to the four groups of launch Mach numbers used in the range firings. These trajectories are shown in Figs. 13–16. The computed spin histories fall within the range of the range data at both of the measurement locations. The computed trajectories show that at the second measurement station, the projectile is within 3% of the steady-state spin rate.

As was discussed, the steady-state spin rate and the roll-producing and roll-damping moment coefficients were determined from the range measurements. The comparison between range and computed values of these parameters is made in Figs. 17–19.

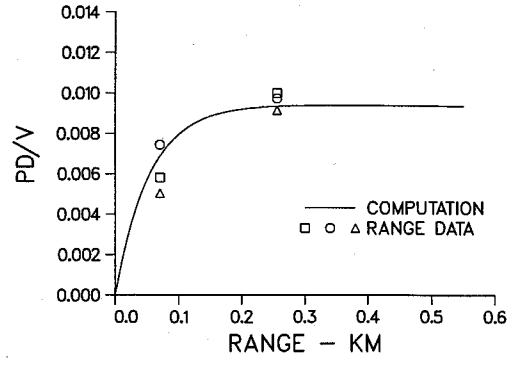

Fig. 13 Comparison computed roll history with range data, launch Mach number = 3.50.

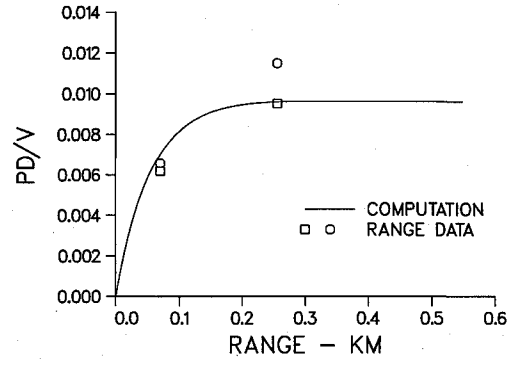

Fig. 14 Comparison computed roll history with range data, launch Mach number = 4.00.

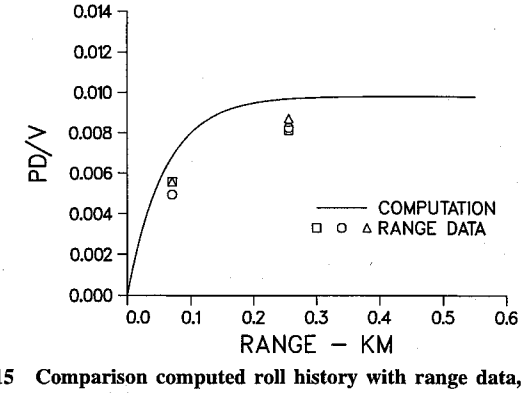

Fig. 15 Comparison computed roll history with range data, launch Mach number = 4.65.

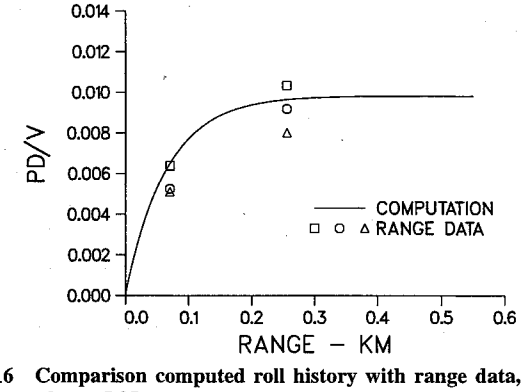

Fig. 16 Comparison computed roll history with range data, launch Mach number = 5.25.

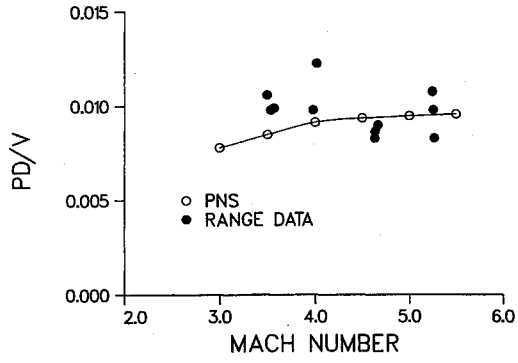

Fig. 17 Comparison of computed Mach number variation of equilibrium spin rate with range data.

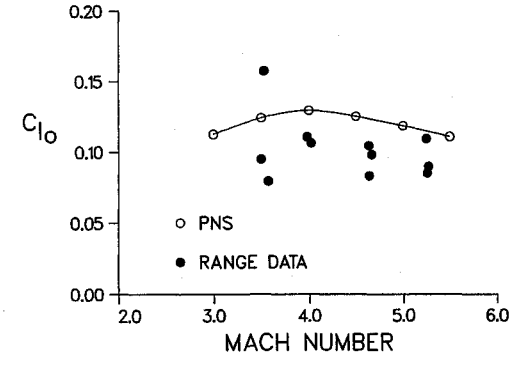

Fig. 18 Comparison of computed Mach number variation of roll-producing moment coefficient with range data.

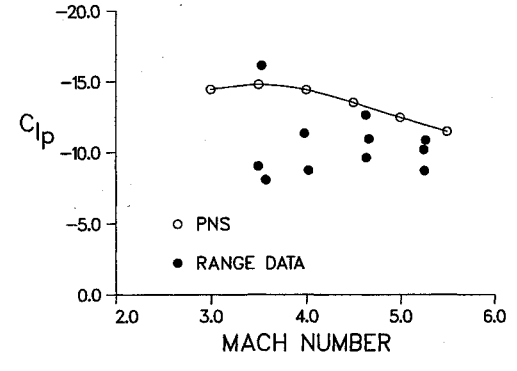

Fig. 19 Comparison of computed Mach number variation of roll-damping moment coefficient with range data.

Figure 17 shows the comparison of the steady-state spin rate as a function of Mach number. The computed results are bracketed by the range data, demonstrating that the predictions of the steady-state spin rate are within the accuracy of measurements.

Comparisons of the roll-producing and roll-damping moment coefficients are shown in Figs. 18 and 19. The computed results for both coefficients lie somewhat above the range data. At Mach 5.25, the range values of the roll-producing moment coefficient are 4–35% below the computed result, whereas the range values of the roll-damping moment coefficient are 10–38% below the computed value. The result that both coefficients show similar comparisons between range and computed values is a reflection of the fact that the steady-state spin rate is approximately the ratio of the roll-producing moment coefficient to the roll-damping moment coefficient. As was shown in Fig. 17, this ratio is accurately predicted.

It has been noted by other investigators[15] that some of the round-to-round variability in the spin history of the projectile can be traced to variability in the fin geometry (particularly the beveled surfaces) that occur during manufacturing. These variations should primarily impact the roll-producing moment coefficient. However, this does not appear to be a significant factor in the range results examined in this report, because similar variations are seen in both the roll-producing and roll-damping moment coefficients.

Some of the variability in the range values of roll-producing and roll-damping moment coefficient can be traced to the measurement of the spin rate at the two measurement stations. For example, it can be shown that a ±10% variation in the roll rate at the first measurement location will result in about a ±20% variation in the roll-producing or roll-damping moment coefficients. Improvements in the determination of the roll coefficients can be made by adding additional measurement stations.

Conclusion

The roll characteristics of a finned projectile have been determined using a computational fluid dynamics approach. The technique makes use of a body-fixed rotating coordinate frame that rotates at the spin rate of the body. The approach allows the steady flow equations to be applied provided the governing equations are appropriately modified to account for the Coriolis and centrifugal accelerations. From the computed flowfield, the aerodynamic moments associated with the roll are determined. The predictions of the roll-producing, roll-damping, and equilibrium spin rate, as well as the predicted spin histories, have been compared with results obtained using engineering estimation approaches and with data obtained from range firings.

The computed steady-state roll rate and the spin histories agree well with the values obtained from range firings. The predicted roll-producing moment and roll-damping moment coefficients lie somewhat above most of the range data although the results show that the time constant for the spin-up process is accurately predicted. The efficiency of the computational approach is sufficient to allow its application in the design cycle. The computational approach appears to provide better estimates of the roll characteristic than the engineering approach, although the engineering approach does allow reasonable estimates of the roll characteristics, particularly for preliminary design studies.

References

[1]Wardlaw, A. B., Jr., Priolo, F. J., and Solomon, J. M., "Multiple-Zone Strategy for Supersonic Missiles," *Journal of Spacecraft and Rockets*, Vol. 24, No. 4, 1987, pp. 377–384.

[2]Oberkampf, W. L., "Prediction of Roll Moments on Finned Bodies in Supersonic Flow," *Journal of Spacecraft and Rockets*, Vol. 12, No. 1, 1975, pp. 17–21.

[3]Prakash, S., and Khurana, D. D., "A Simple Estimation Procedure of Roll-Rate Derivatives for Finned Vehicles," *Journal of Spacecraft and Rockets*, Vol. 21, No. 3, 1984, pp. 318–320.

[4]Eastman, D. W., "Roll Damping of Cruciform-Tailed Missiles," *Journal of Spacecraft and Rockets*, Vol. 23, No. 1, 1986, pp. 119, 120.

[5]Mikhail, A. G., "Roll Damping for Projectiles Including Wraparound, Offset, and Arbitrary Number of Fins," *Journal of Spacecraft and Rockets*, Vol. 32, No. 6, 1995, pp. 929–937.

[6]Devan, L., "Nonaxisymmetric Body, Supersonic, Inviscid Dynamic Derivative Prediction," *Proceedings of the AIAA 7th Applied Aerodynamics Conference*, AIAA, Washington, DC, 1989 (AIAA Paper 89-2195).

[7]Murphy, C. H., "Free Flight Motion of Symmetric Missiles," U.S. Army Ballistic Research Lab., Rept. 1216, Aberdeen Proving Ground, MD, July 1963, pp. 18–21.

[8]Schiff, L. B., and Steger, J. L., "Numerical Simulation of Steady Supersonic Viscous Flow," *AIAA Journal*, Vol. 18, No. 12, 1980, pp. 1421–1430.

[9]Baldwin, B. S., and Lomax, H., "Thin Layer Approximation and Algebraic Model for Separated Turbulent Flows," AIAA Paper 78-257, Jan. 1978.

[10]Beam, R., and Warming, R. F., "An Implicit Factored Scheme for the Compressible Navier–Stokes Equations," *AIAA Journal*, Vol. 16, No. 4, 1978, pp. 85–129.

[11]Rai, M. M., and Chaussee, D. S., "New Implicit Boundary Procedure: Theory and Applications," AIAA Paper 83-0123, Jan. 1983.

[12]Rai, M. M., Chaussee, D. S., and Rizk, Y. M., "Calculation of Viscous Supersonic Flows over Finned Bodies," AIAA Paper 83-1667, July 1983.

[13]Nielsen, J. N., *Missile Aerodynamics*, McGraw–Hill, New York, 1960, pp. 15, 16.

[14]Liepmann, H. W., and Roshko, A., *Elements of Gasdynamics*, Wiley, New York, 1957, pp. 109–113.

[15]Brandon, F. J., private communication, U.S. Army Ballistic Research Lab., Aberdeen Proving Ground, MD, Jan. 1989.

R. M. Cummings
Associate Editor